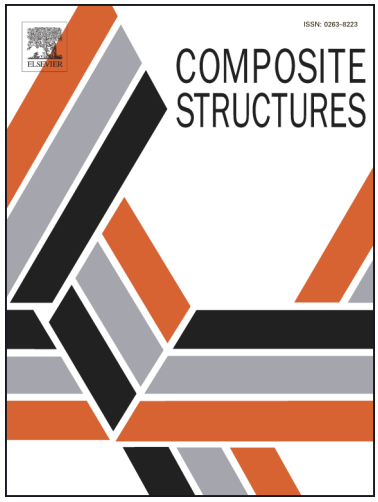

Performance of frequency and/or phase modulated excitation waveforms for optical infrared thermography of CFRPs through thermal wave radar: A simulation study

Saeid Hedayatrasa, Gaétan Poelman, Joost Segers, Wim Van Paepegem, Mathias Kersemans

PII: S0263-8223(19)30729-9
DOI: https://doi.org/10.1016/j.compstruct.2019.111177
Article Number: 111177
Reference: COST 111177

To appear in: *Composite Structures*

Received Date: 26 February 2019
Revised Date: 5 June 2019
Accepted Date: 18 June 2019

Please cite this article as: Hedayatrasa, S., Poelman, G., Segers, J., Van Paepegem, W., Kersemans, M., Performance of frequency and/or phase modulated excitation waveforms for optical infrared thermography of CFRPs through thermal wave radar: A simulation study, *Composite Structures* (2019), doi: https://doi.org/10.1016/j.compstruct.2019.111177

Performance of frequency and/or phase modulated excitation waveforms for optical infrared thermography of CFRPs through thermal wave radar: A simulation study

Saeid Hedayatrasa [1,2*], Gaétan Poelman[1,2], Joost Segers[1], Wim Van Paepegem[1] and Mathias Kersemans[1]

[1] Mechanics of Materials and Structures (UGent-MMS), Department of Materials, Textiles and Chemical Engineering, Ghent University, Technologiepark-Zwijnaarde 46, 9052 Zwijnaarde, Belgium

[2]SIM Program M3 DETECT-IV, Technologiepark-Zwijnaarde 48, B-9052 Zwijnaarde, Belgium

[*]saeid.hedayatrasa@ugent.be

Abstract

Following the developments in pulse compression techniques for increased range resolution and higher signal to noise ratio of radio wave radar systems, the concept of thermal wave radar (TWR) was introduced for enhanced depth resolvability in optical infrared thermography. However, considering the highly dispersive and overly damped behavior of heat wave, it is essential to systematically address both the opportunities and the limitations of the approach. In this regard, this paper is dedicated to a detailed analysis of the performance of TWR in inspection of carbon fiber reinforced polymers (CFRPs) through frequency and/or phase modulation of the excitation waveform. In addition to analogue frequency modulated (sweep) and discrete phase modulated (Barker binary coded) waveforms, a new discrete frequency-phase modulated (FPM) excitation waveform is introduced. All waveforms are formulated based on a central frequency so that their performance can be fairly compared to each other and to lock-in thermography at the same frequency. Depth resolvability of the waveforms, in terms of phase and lag of TWR, is firstly analyzed by an analytical solution to the 1D heat wave problem, and further by 3D finite element analysis which takes into account the anisotropic heat diffusivity of CFRPs, the non-uniform heating induced by the optical source and the measurement noise. The spectrum of the defect-induced phase contrast is calculated and, in view of that, the critical influence of the chosen central frequency and the laminate's thickness on the performance of TWR is discussed. Various central frequencies are examined and the outstanding performance of TWR at relatively high excitation frequencies is highlighted, particularly when approaching the so-called blind frequency of a defect.

Keywords**:** Infrared Thermography, Optical, Radar, Waveform, Pulse Compression, CFRP, Composite

1 Introduction

Fiber reinforced polymers offer great advantages for structural applications (e.g. high specific stiffness, corrosion resistance and adjustable anisotropy) which has made them one major alternative to replace the traditional metallic components, particularly in the aerospace sector. However, their layer-wise and non-homogenous microstructure makes them prone to initiation and propagation of multiple defect types during production and operational life. This has given rise to

the need for the development of reliable non-destructive testing (NDT) techniques in order to ensure both a high safety level and a low maintenance cost.

Fundamentally, in most advanced NDT techniques the inspection surface is exposed to an excitation (elastic, acoustic, electromagnetic or heat) incident energy and the defects are detected based on their interaction with the corresponding wave field. Among various techniques, infrared thermography has attracted considerable industrial interest because of its capability to inspect relatively large surfaces, quickly and remotely, through the full-field thermal images recorded by an infrared camera [1]. In optical infrared thermography the heat wave is normally stimulated by radiation from an optical source (i.e. halogen or flash lamps) which then travels through the thickness of the component and reveals the defects based on their thermal diffusivity mismatch. The inspection may be performed in reflection or transmission mode. Although the transmission mode has deeper detection depth [2], it is not the preferred mode of inspection due to its required access to the backside of the specimen.

Non-uniform heating introduced by the optical source and the non-uniform and directional emissivity of the inspection surface are important limiting factors of optical infrared thermography which degrade the quality of the measured thermal images. Moreover, the technique is limited by the diffusive nature of the heat wave as its amplitude exponentially decays over space and (contrary to elastic waves) lacks a wavefront to provide high incident energy. This is due to the absorption of heat along the diffusion path which results in an overly-damped non-propagating response. Therefore, a defect has to be close enough to the surface (in the order of diffusivity length) to be detectable. In this case, the excitation heat wave (after traveling to the defect's interfaces and back to the surface while experiencing a 3D heat diffusion) is able to provide a localized measurable discrepancy in the thermal response of defected and sound area.

The development of adequate excitation and post-processing techniques to overcome the aforementioned detectability limits of optical infrared thermography has been widely researched [3-12]. Principally, temporal and spectral shaping of the excitation waveform can control its effective diffusion length and corresponding thermal response in order to achieve improved defect-induced contrast and deeper detection range. Moreover, derivative and phase delay analysis of the thermal response enables the calculation of quantities with minimal sensitivity to the non-uniformity of absorbed/emitted heat magnitude (so-called emissivity-normalized) or quantities with an earlier indication of defects (i.e. least influence by 3D heat diffusion).

Lock-in thermography (LT) and pulsed thermography are the two fundamental approaches of optical infrared thermography [13, 14]. In LT a harmonic excitation is applied to the sample at a certain frequency for a number of cycles which results in heat penetration deep into the corresponding diffusion length. The amplitude and phase of the thermal response during heating are then calculated, which the latter is an emissivity-normalized quantity. However, LT is based on a mono-frequency excitation and the defects having their thermal response in-phase with the sound area (i.e. excited at the so-called blind frequency) are transparent in the resultant phase image. In pulsed thermography the sample is subjected to a very short time (i.e. broadband) pulse of a few milliseconds using a high energy flash lamp and the thermal evolution of the surface is observed during the post-flash cooling stage. However, the short duration of the pulse leads to a high sensitivity to shallow defects (i.e. enriched high-frequency response) and a low sensitivity to deep defects (i.e. poor low-frequency response). More recently, long-pulse thermography was

proposed [15, 16] in which a relatively long step heating of a few seconds is applied which leads to an increased probing depth compared to pulsed thermography. Contrary to step heating thermography [17], which is based on the analysis of the heating stage, long pulse thermography is performed by observation and post-processing of the cooling stage (similar to pulsed thermography).

Mulaveesala, Vaddi [18] introduced the application of an analogue frequency modulated (sweep) excitation waveform for enhanced depth resolvability of optical infrared thermography. A steel sample with flat bottom holes (FBHs) was inspected and the efficiency of approach in detection of defects was demonstrated. The technique was inspired by the pulse compression technique used for increased signal to noise ratio (SNR) of radar systems. Matched filtering of the reflected echo from a target (i.e. defects in infrared thermography) with the excitation signal, compresses its energy under the main lobe and increases the SNR without loss of resolution compared to a short pulse radar. The delay time of the main lobe's peak (i.e. lag) exploits an indication of the defect's depth in the presence of the excitation/measurement noises.

Tabatabaei and Mandelis [19] performed an in-depth analytical and experimental study on establishing the concept of thermal wave radar (TWR) using a sweep excitation. The effect of sweep bandwidth and band limits on depth resolvability was studied, and its increased SNR compared to LT (at the highest frequency of the sweep's bandwidth) was shown. The phase of TWR was later introduced [20] as an emissivity-normalized quantity with increased depth resolvability resolution compared to LT phases at the two (lower and upper) band limits of the sweep excitation. The enhanced depth resolvability of TWR using Barker binary coded (i.e. discrete phase modulated) excitation waveforms was further studied by Tabatabaei and Mandelis [21] and the capability of this technique in deconvolution of superposed thermal responses from overlapping defects was experimentally demonstrated in a follow-up study [22]. TWR with truncated-correlation has also been introduced for photo-thermal tomography and 3D reconstruction of deep defects [23, 24].

The promise of TWR in optical infrared thermography also attracted interest in its implementation for NDT of composite materials. Ghali, Panda [25] investigated the efficiency of Barker coded TWR in the inspection of carbon fiber reinforced composites (CFRPs) with FBHs and presented improved SNR of lag images at particular time instance compared to the phase of FFT. Gong, Liu [26] investigated the performance of TWR in the inspection of a CFRP coupon with FBHs subject to a sweep excitation and compared phase and lag of TWR with FFT phase images (at certain frequencies inside the sweep bandwidth) in terms of SNR and defect-induced contrast. It was concluded that for the deepest defect phase of TWR outperforms the rest, and for the shallowest defect, FFT phase at a chosen frequency outperforms phase and lag images of TWR. TWR with a Barker coded step excitation was applied to a CFRP coupon with teflon inserts (as artificial delaminations) by Silipigni, Burrascano [27] and improved strategies were suggested for increased SNR of amplitude images. Most recently, Shi, Liu [28] studied inspection of a CFRP coupon with FBHs using TWR with Barker coded excitations of different code lengths and different carrier frequencies. According to the results, a 5-bits Barker code showed the highest SNR of lag and phase of TWR, and it was shown that the phase of TWR outperforms LT phase for the deepest defects of the investigated test piece. Other studies have also been dedicated to

evaluating the efficiency of frequency and amplitude modulation schemes [29, 30] and optimization of filters for reduced side-lobes [31, 32].

With regards to the existing literature regarding the efficiency of TWR, it is believed that further research is vital in order to set the expected performance and limitations of the technique particularly for NDT of composite materials. To this end, this paper is dedicated to a detailed analysis of the performance of TWR in the inspection of CFRPs through different modulated waveforms. In addition to analogue frequency modulated (sweep) and discrete phase modulated (Barker binary coded) waveforms, a new discrete frequency-phase modulated excitation waveform is also introduced as a potential alternative for pulse compression. A 10 plies 2.9 mm thick unidirectional CFRP laminate is studied using a simplified 1D analytical solution to the thermal wave problem and further by a full 3D finite element (FE) analysis. Depth resolvability of the three waveform types in the inspection of the delaminations of different depths is evaluated at multiple central frequencies. The spectrum of defect-induced phase contrast is calculated and the critical influence of chosen central frequency and laminate's thickness on the performance of TWR is discussed and compared to LT at the same frequency.

The structure of the paper is as follows. In section 2 the theory of TWR and pulse compression technique are discussed, then the modulated waveforms are defined and their depth resolvability is analyzed based on the analytical solution. The details of the FE modeling and the corresponding results are presented and discussed in section 3. Concluding remarks are given in section 4.

2 Thermal wave radar using frequency and/or phase modulated waveforms

Radar is an abbreviation for "Radio Detection And Ranging" which is a system that transmits electromagnetic radio waves for determining the range, speed and location of targets based on their reflected echo [33]. Old pulsed radars used a very short pulse for higher detectability of overlapping echoes of multiple defects (i.e. higher range resolution) and suffered from very low energy of the pulse and resultant low SNR. Then pulse compression emerged as an alternative technique which enables transmission of long bursts without loss of range resolution. The technique is based on frequency and/or phase modulation of the burst which can further be compressed through matched filtering [34].

TWR takes the advantage of pulse compression technique to use wideband modulated waveforms for enhanced depth resolvability range and resolution of infrared thermography. Contrary to original radar application, TWR deals with the dispersive and non-propagating (diffusive) thermal response of the test piece that causes significant distortion of the response compared to its excitation waveform. Moreover, the excitation source in TWR is a mono-polar (heating) source which always includes an unfavorable DC component leading to global heating of the test piece during excitation. This necessitates proper filtering of the DC component of the thermal response before matched filtering. However, this is ideally performed in the analytical solution by applying bi-polar (heating and cooling) AC excitation waveforms.

2.1 Heat wave diffusion in CFRPs and 1D analytical solution

Heat diffusion in an anisotropic solid, in the absence of internal heating, is defined by the following parabolic differential equation:

$$\nabla \cdot (\boldsymbol{\alpha} \cdot \nabla T(\mathbf{r},t)) - \frac{\partial T(\mathbf{r},t)}{\partial t} = 0 \quad (1)$$

where T is temperature [K], t is time [s], $\mathbf{r} = [x\ y\ z]$ is the spatial vector [m], ∇ is the nabla gradient operator, and $\boldsymbol{\alpha}$ is the tensor of anisotropic thermal diffusivity [m^2/s] defined as:

$$\boldsymbol{\alpha} = \frac{\mathbf{k}}{\rho c_p} \quad (2)$$

Here $\mathbf{k}$ is the second order tensor of anisotropic conductivity [W/m.K], ρ is density [kg/m^3] and c_p is heat capacity [J/kg.K] at constant pressure. Subsequently, assuming a harmonic solution of $T(\mathbf{r},t) = \theta(\mathbf{r},\omega)\exp(i\omega t)$, the Equation 1 reduces to:

$$\nabla \cdot (\boldsymbol{\alpha} \cdot \nabla \theta(\mathbf{r},\omega)) - i\omega\, \theta(\mathbf{r},\omega) = 0 \quad (3)$$

where $\omega = 2\pi f$ is the angular frequency [1/s] and $i = \sqrt{-1}$. By assuming a 1D heat diffusion through the thickness of a homogeneous solid, the Equation 3 reduces to:

$$\frac{\partial^2 \theta(z,\omega)}{\partial z^2} - \beta^2 \theta(z,\omega) = 0 \quad (4)$$

By defining through-the-thickness diffusivity length as $\mu_z(\omega) = \sqrt{2\alpha_z/\omega}$ then $\beta(\omega) = \sqrt{i\omega/\alpha_z} = (1+i)/\mu_z(\omega)$.

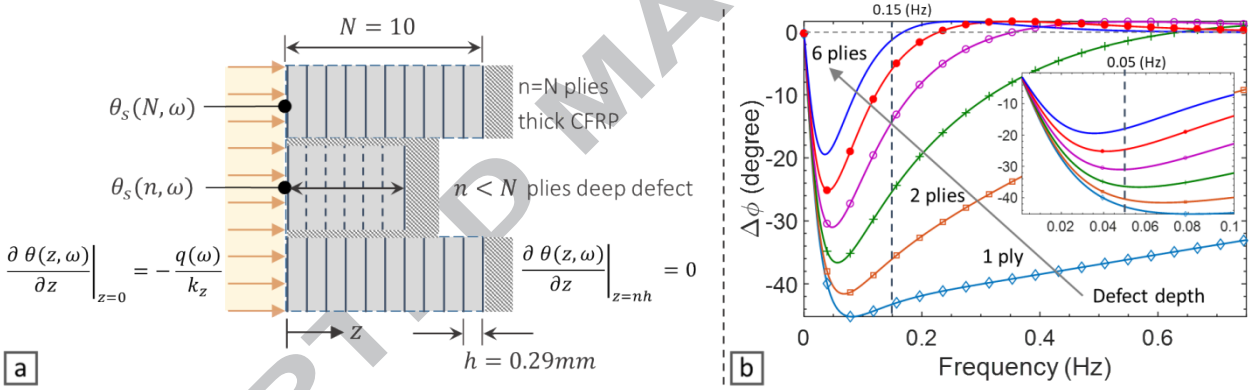

Figure 1: (a) simplified 1D definition of thermal wave diffusion through the thickness of a $N = 10$ plies CFRP laminate with defects as shallower ($n < N$ plies) reflectors in which shaded boundaries indicate thermal isolation, and (b) corresponding spectrum of the defect-induced phase contrast at inspection surface ($z = 0$)

The 1D model of a $N = 10$ plies CFRP laminate and corresponding boundary conditions are schematically shown in Figure 1(a), in which defects (i.e. delaminations) are introduced as shallow reflectors of $n < N$ plies thick (each ply $h = 0.29$ mm thick). The inspection surface is subjected to an excitation heat amplitude $q(\omega)$, there is no heat dissipation from the backside and no thermal interaction at the lateral faces of each component. Equation 4 is a homogenous second order partial differential equation with the solution:

$$\theta(z,\omega) = A\exp(\beta(\omega)z) + B\exp(-\beta(\omega)z) \quad (5)$$

By applying the boundary conditions provided in Figure 1(a), the coefficients A and B for an n plies thick CFRP are calculated as:

$$A = \frac{q(\omega)}{\beta(\omega)k_z} \frac{\exp(-2\beta(\omega)nh)}{1-\exp(-2\beta(\omega)nh)} \quad (6)$$

$$B = \frac{q(\omega)}{\beta(\omega)k_z}\frac{1}{1-\exp\left(-2\beta(\omega)nh\right)} \tag{7}$$

Consequently, the thermal frequency response at the inspection surface (i.e. $z = 0$) is:

$$\theta_s(n,\omega) = A(n,\omega) + B(n,\omega) \tag{8}$$

in which the number of plies n is introduced as an additional variable to take into account the effect of the laminate's thickness (or the reflector's depth) on the surface temperature θ_s. Therefore, the thermal phase contrast with respect to the sound area (i.e. $n = N$) can be calculated as:

$$\Delta\varphi(n,\omega) = \tan^{-1}\left(\frac{Im(\theta_s(n,\omega))}{Re(\theta_s(n,\omega))}\right) - \tan^{-1}\left(\frac{Im(\theta_s(N,\omega))}{Re(\theta_s(N,\omega))}\right) \;;\; n \le N \tag{9}$$

For a given excitation signal $S(t)$ and heating amplitude q_0, the relevant heating load in frequency-domain is calculated as:

$$q(\omega) = \mathcal{F}\{q_0 S(t)\} \tag{10}$$

and the corresponding time-domain thermal response at the inspection surface is derived by:

$$T_s(n,t) = \mathcal{F}^{-1}\{\theta_s(n,\omega)\} \tag{11}$$

Here $\mathcal{F}$ and $\mathcal{F}^{-1}$ denote Fourier and inverse Fourier transform operators, respectively.

The resultant spectrum of the defect-induced phase contrast (herein called phase spectrum for convenience) is shown in Figure 1(b), in which the through-the-thickness diffusivity of $\alpha_z = 6.16 \times 10^{-7}\ \mathrm{m}^2/\mathrm{s}$ is assumed for the CFRP [35]. The results are shown for reflectors which are 1 to 6 plies deep (0.29 To 1.74 mm depth). These depths also correspond to the depths of delaminations considered in section 3 for FE simulation. The phase spectrum indicates the lower phase contrast and lower blind frequency (i.e. first zero-crossing) of deeper defects. The frequency response at an excitation frequency of 0.05 Hz leads to a very high phase contrast as it is close to the dips associated with the maximum phase contrast of relatively deep defects. However, a frequency of 0.15 Hz significantly reduces the phase contrast of deep defects and provides a very poor indication of the deep defect. In this section, these two frequencies are selected as reference frequencies to evaluate the efficiency of TWR under corresponding strong and poor contrast conditions.

2.2 Matched filtering of the thermal response

Matched filter is an optimal linear filter that maximizes the SNR of the measured response at its output at a delay time τ_M, corresponding to the depth of the defect, in the presence of the excitation/measurement noises. Matched filtering is usually done by time-domain cross-correlation (CC) of a measured thermal response $\tilde{T}(t)$ with corresponding excitation (reference) waveform $\tilde{S}(t)$ as follows:

$$\chi(\tau) = \tilde{T}(t) \otimes \tilde{S}(t+\tau) = \int_{-\infty}^{+\infty} \tilde{T}(t)\tilde{S}(t+\tau)dt \tag{12}$$

where $\otimes$ denotes CC and $\tilde{(\,)}$ denotes the AC component of the signal. For computational efficiency CC is performed in the frequency-domain as:

$$\chi(\tau) = \mathcal{F}^{-1}\{\vartheta(\omega)\varsigma^{*}(\omega)\} \quad (13)$$

$$\vartheta(\omega) = \mathcal{F}\{\tilde{T}(t)\} \quad (14)$$

$$\varsigma(\omega) = \mathcal{F}\{\mathrm{W}(t)\tilde{S}(t)\} \quad (15)$$

where (*) denotes the complex conjugate and W is a windowing function (e.g. Hanning window) used for reducing side lobes when performing CC in the frequency-domain. When using the analytical frequency response of section 2.1 (in which the thermal response is calculated for an AC excitation), $\vartheta(\omega) = \theta_s(n,\omega)$ and $\varsigma(\omega) = q(\omega)/q_0$. The output of CC operation $\chi(\tau)$ is a sinc like function which compresses the energy of the whole signal under its main peak. The peak-sidelobe-level, i.e. the ratio of the sidelobe level to the main lobe, indicates the quality of pulse compression (see Figure 3). A lower peak-sidelobe-level implies a lower noise level and consequently a higher SNR in the output of CC. The lag of CC's main lobe is an emissivity-normalized quantity corresponding to the defect's depth, which is defined as:

$$lag_{\chi} = \tau|_{\chi(\tau) = \mathrm{Max}(\chi(\tau))} \quad (16)$$

Subsequently, the phase of CC denoted as φ_{χ} can be found (as another emissivity-normalized quantity) by repeating the operation with a new reference waveform using Hilbert transform so that all its spectral components are -90° degree phase shifted:

$$\varsigma_H(\omega) = \mathcal{F}\{\mathrm{W}(t)\mathcal{H}(\tilde{S}(t))\} = -i\mathrm{sgn}(\omega)\varsigma(\omega) \quad (17)$$

$$\chi_H(\tau) = \mathcal{F}^{-1}\{\vartheta(\omega)\varsigma_H^{*}(\omega)\} \quad (18)$$

$$\varphi_{\chi} = \tan^{-1}\left(\frac{\chi(\tau)}{\chi_H(\tau)}\right)\Bigg|_{\tau=0} \quad (19)$$

where sgn denotes the sign function. Obviously, in case of mono-frequency harmonic excitation, the calculated CC-phase reduces to the phase of LT.

2.3 Definition of excitation waveforms

The performance of a radar's waveform is determined based on its range (and Doppler) resolution which depends on the ambiguity in detecting overlapping echoes in the presence of stochastic noise. Various modulated waveforms with analogue or discrete modulation have been developed for radar application e.g. analogue frequency modulation (sweep), discrete frequency modulation (Costas coding), discrete phase modulation (e.g. Barker binary coding or poly-phase Frank coding) or an arbitrary modulation achieved by optimization [34, 36].

In this study, in addition to the Barker coded and frequency modulated sweep waveforms which have already been considered for TWR application in the literature, a new discrete frequency-phase modulated (FPM) excitation is introduced. All considered waveforms are defined based on a central frequency f_c so that their performance can be evaluated and compared to each other, as well as to LT at this central frequency f_c. The three modulated waveforms for a central frequency $f_c = 0.15$ Hz and corresponding thermal response (calculated by Equation 11) for a 6 plies deep CFRP reflector (corresponding to the deepest defect considered further on for FE simulation) are given in Figure 2. A descending frequency modulation rate is applied so that the

specimen's depth is consistently resolved by the increasing diffusion length of the excited thermal waves.

2.3.1 Discrete Barker phase modulation

The Barker phase modulated waveform [34] is defined as a harmonic signal of carrier frequency (i.e. the central frequency) f_c with 180 degree phase shift at certain cycles, applied through a binary code:

$$C = \begin{cases} [1,1,\ 1,1,\ 1,-1,-1,1,1,-1,1,-1,1\ ] \ ;\ 13 \text{ bits } (m=13) \\ [1,1,1,-1,1] \ ;\ 5 \text{ bits } (m=5) \\ [1,1,-1] \ ;\ 3 \text{ bits } (m=3) \end{cases} \quad (20)$$

$$P_j(\mathrm{t}) = \begin{cases} 1 \ ; \ (j-1)/f_c \le t < j/f_c \\ 0 \ ; \ else \end{cases} \quad (21)$$

$$\tilde{S}_1(t) = \sum_{j=1}^{m} P_j(\mathrm{t}) \cos\left(2\pi f_c t + \frac{\pi}{2} C_j\right) \quad (22)$$

where C is the Barker binary phase code in which each bit corresponds to a single harmonic cycle of $1/f_c$ long. Different Barker code lengths are introduced in the literature, of which the 13 bits code is known to have the lowest peak-sidelobe-level (see Figure 2(a) for $f_c = 0.15$ Hz). In this study also shorter code lengths of 3 and 5 bits are considered to compare their peak-sidelobe-level.

2.3.2 Analogue linear sweep modulation

Narrowband and wideband linear frequency modulated sweeps are also considered around the central frequency f_c and a total burst time of $t_b = 15/f_c$ is assumed (see Figure 2(b) for the wideband sweep of 100 s at $f_c = 0.15$ Hz). The sweep signal is defined as:

$$[f_1, f_2] = \begin{cases} [f_c(1+0.33), f_c(1-0.33)] \ ;\ \text{Narrowband} \\ [f_c(1+0.66), f_c(1-0.66)] \ ;\ \text{Wideband} \end{cases} \quad (23)$$

$$f(t) = f_1 + \left(\frac{f_2 - f_1}{2t_b}\right) t \quad (24)$$

$$\tilde{S}_2(t) = cos\,(2\pi f(t).t - \pi) \quad (25)$$

2.3.3 Discrete frequency-phase modulation (FPM)

Moreover, a novel narrowband FPM waveform is introduced with a total burst time of $t_b = 15/f_c$ and a discrete frequency and phase modulation as follows:

$$[f_1, f_2] = [f_c(1+0.33), f_c(1-0.33)] \ ;\ \text{Narrowband} \quad (26)$$

$$\boldsymbol{C_f} = [1.00\ \ 0.89\ \ 0.78\ \ 0.67\ \ 0.56\ \ 0.44\ \ 0.33\ \ 0.22\ \ 0.11\ \ 0.00] \quad (27)$$

$$\boldsymbol{f} = f_1 + (f_2 - f_1)\,\boldsymbol{C_f} \quad (28)$$

$$\boldsymbol{\varphi} = \frac{\pi}{2}[-0.94, +1.11, -0.88, -1.54, +0.34, +0.67, -0.30, +1.16, +1.05, -0.33] \quad (29)$$

$$\tilde{S}_3(t) = \sum_{j=1}^{10} P_j(\mathrm{t}) \cos\left(2\pi f_j t + \varphi_j\right) \quad (30)$$

The frequency code $\boldsymbol{C_f}$ splits the waveform into 10 sub-pulses such that each sub-pulse has a constant frequency equally stepped from f_1 to f_2. In this way each sub-pulse includes at least one complete harmonic cycle (among which the last sub-pulse with lowest frequency of $f_2 = f_c (1 - 0.33)$ includes one complete harmonic cycle). The phase of sub-pulses is also discretely shifted by the vector $\boldsymbol{\varphi}$ given in Equation 29 (see Figure 2(c) for the FPM waveform of 100 s at $f_c = 0.15$ Hz). This phase vector is determined by examining a population of 50,000 excitation waveforms with randomly generated phase vectors in the range $\left[-\frac{\pi}{2}, +\frac{\pi}{2}\right]$. The phase vector which yields the lowest peak-sidelobe-level is chosen for the FPM signal.

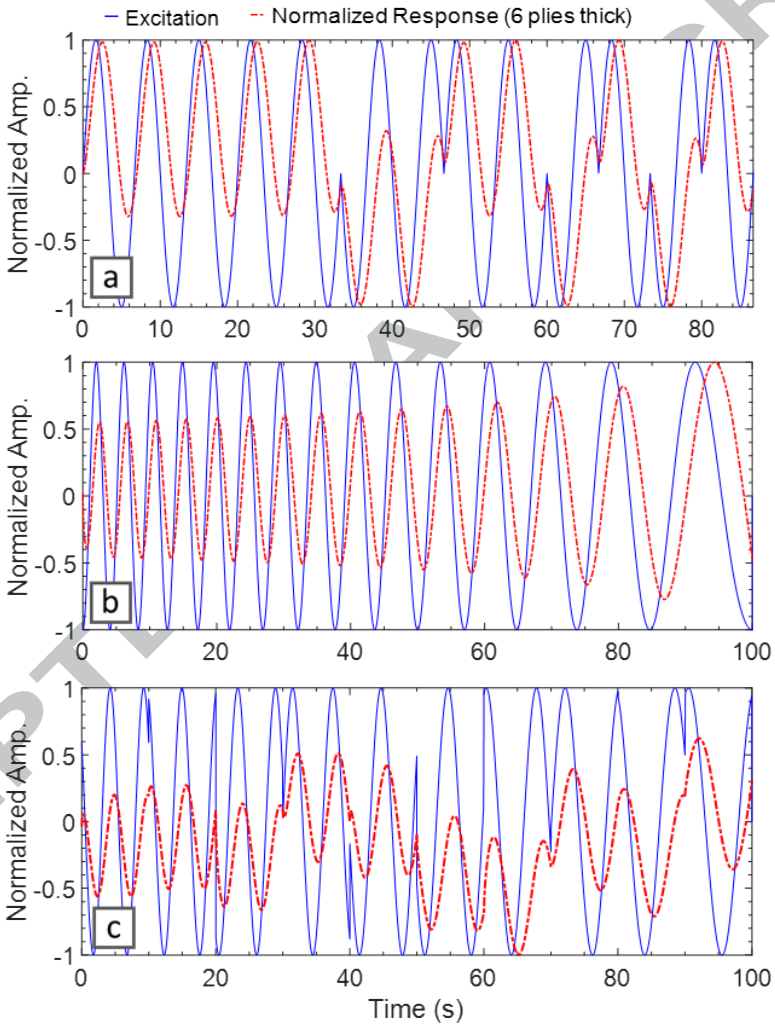

Figure 2: Waveform types used for TWR analysis (a) 13 bits Barker binary phase coded, (b) linear frequency modulated sweep and (c) newly introduced FPM waveform with discrete frequency-phase modulation, shown for a central frequency of $f_c = 0.15$ Hz along with corresponding thermal responses from a reflector of 6 plies deep (corresponding to the deepest (1.74 mm deep) defect considered further on for FE simulation) calculated by Equation 11

2.4 Depth resolvability of excitation waveforms

The CC of the modulated waveforms introduced in Figure 2 and corresponding thermal response for a 6 plies deep CFRP reflector (i.e. $\vartheta(\omega) = \theta_s(6,\omega)$ corresponding to the deepest delamination modelled in FE simulation) and resultant peak-sidelobe-levels are presented in Figure 3, at the central frequency 0.15 Hz. The main lobe's peak occurs at a lag time $\tau_M > 0$ as indicated in the inset of Figure 3(a). It is further shown how waveform modulation leads to pulse compression and lowers the sidelobe level compared to a normal LT with mono-frequency harmonic excitation (Figure 3(b)). Among modulated waveforms, the 13 bits Barker code has the highest quality and the narrowband sweep has the lowest quality in terms of peak-sidelobe-level (Figure 3(a)). The FPM waveform exhibits much better performance compared to the narrowband sweep of the same frequency range and has a peak-sidelobe-level comparable to that of wideband sweep (Figure 3(b)).

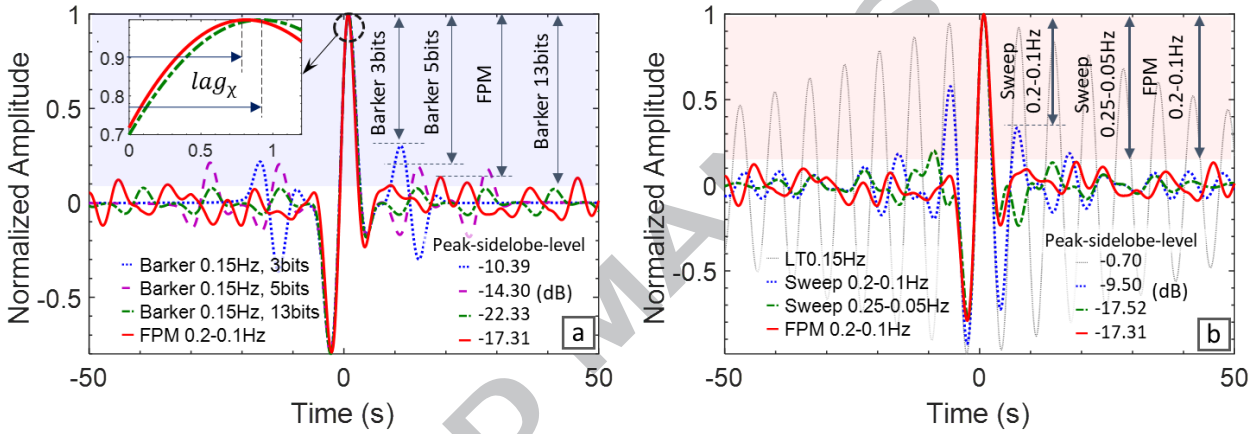

Figure 3: Cross-correlation of excitation waveforms (given in Figure 2) with the corresponding thermal response for a 6 plies thick CFRP at a central frequency of $f_c = 0.15$ Hz , and resultant peak-sidelobe-level in dB

In order to evaluate the depth resolvability of modulated waveforms at the central frequency 0.15 Hz, the gradient of corresponding CC-lag contrast and CC-phase contrast are shown in Figure 4(a) and (b), respectively. Compared to LT, depth resolvability consistently increases by modulation orderly by narrowband sweep, wideband sweep, FPM and ultimately by Barker coding (negligibly affected by the code length). Increased depth resolvability of CC-lag is evident by its magnified contrast throughout the depth and its widened contrast range. On the contrary, the total range of phase contrast is not increased by modulation. In fact, the depth resolvability resolution (i.e. through depth gradient) of the very shallow defects is reduced by (desirably) increased depth resolvability resolution of (hard to detect) deep defects. As for the FPM waveform, despite its comparable peak-sidelobe-level to a wideband sweep, its depth resolvability is significantly higher than wideband sweep and in terms of phase contrast very close to depth resolvability of Barker coded waveform at the deepest defects (see the inset of Figure 4(b)).

Furthermore, the other central frequency of 0.05 Hz is examined at which (according to the phase spectrum shown in Figure 1(b)) a consistently strong phase contrast is expected over the depth particularly for deeper defects. From the results shown in Figure 4(c), it is evident that Barker coding increases depth resolvability of the 10 plies thick laminate in terms of CC-lag. However, depth resolvability of the CC-phase with respect to LT, as shown in Figure 4(d), varies

by the defect's depth. In fact, when inspecting the 10 plies thick laminate at 0.05 Hz, the phase contrast obtained from LT (i.e. without modulation) is higher than the phase contrast obtained from a Barker coded waveform for defects down to 6 plies, though Barker coding outperforms for defects deeper than that.

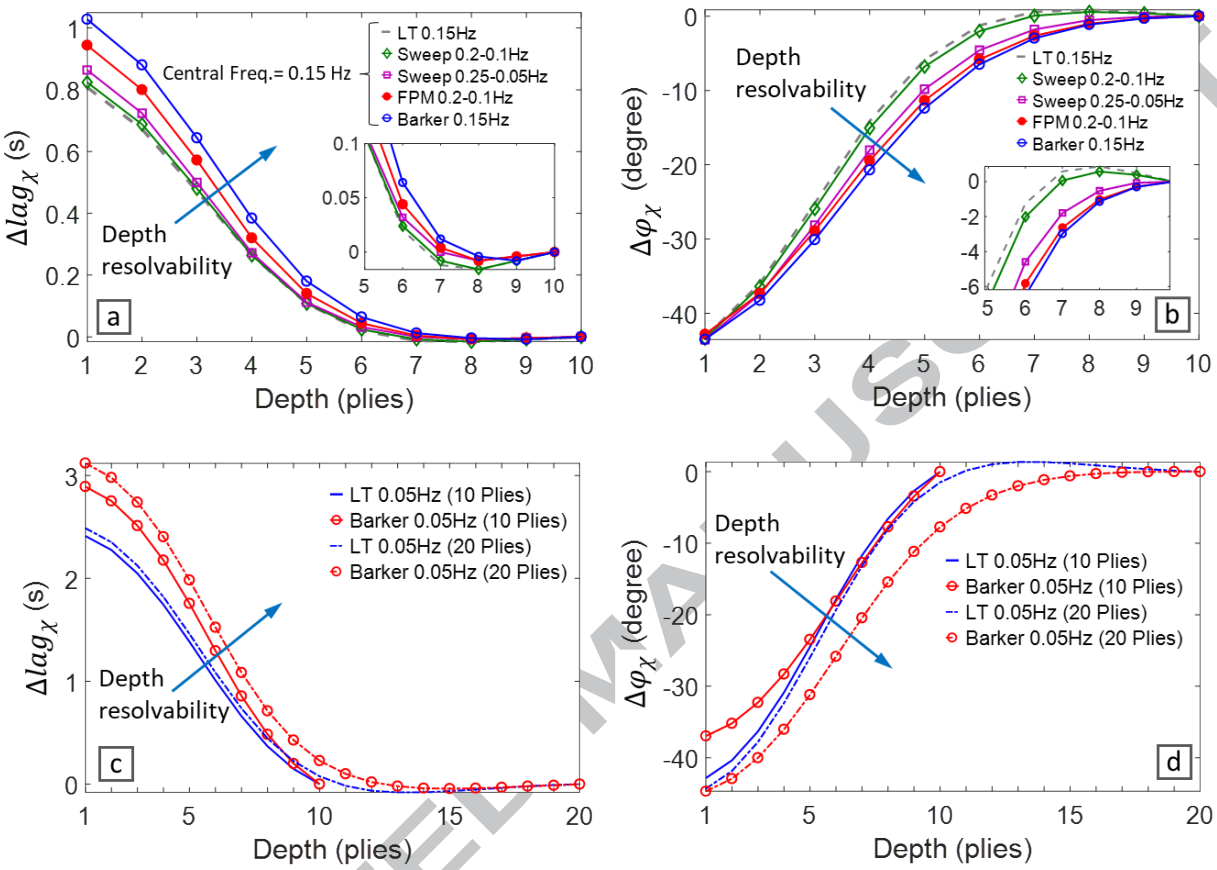

Figure 4: Depth resolvability of excitation waveforms (a,b) at a central frequency of 0.15 Hz for the 10 plies thick CFRP, (c,d) at a central frequency of 0.05 Hz for two different CFRPs of 10 and 20 plies thick; (a,c) CC-lag time contrast and (b,d) CC-phase contrast

Analysis of an additional 20 plies thick laminate at the same central frequency 0.05 Hz (see Figure 4(c,d)) reveals the strong dependency of depth resolvability to the sample's thickness. Figure 4(c) confirms the consistently increasing depth resolvability of CC-lag, regardless of the laminate's thickness. However, according to Figure 4(d), an increased thickness of laminate leads to enhanced depth resolvability of the CC-phase so that the Barker coded waveform outperforms LT throughout the depth. This is due to the fact that the increased thickness makes the phase spectrum distinctively different from the one shown in Figure 1(b)) for the 10 plies CFRP.

Consequently, depth resolvability of CC-phase over the desired depth range (with respect to LT) strongly depends on the corresponding phase spectrum in the vicinity of chosen excitation frequency which is highly affected by the residual thickness of the laminate (from defect to the backside). However, the results confirm that in any case the very deep, and as such the more challenging defects are more robustly resolved through CC-phase of modulated waveforms.

In practice, the efficiency of modulated waveforms depends on both peak-sidelobe-level (Figure 3) and depth resolvability (Figure 4) which determine the robustness in defects detection in the presence of noise. This has been addressed in the following section based on realistic FE simulation.

3 FE simulation of performance in the inspection of CFRPs

The simplified 1D analytical solution presented in section 2 enables fast calculation of the thermal response for a fundamental parametric study and a random search for an FPM waveform with lowest peak-sidelobe-level. However, the 1D approach is valid for thermal diffusion into the defect's interface, only if the inspection surface is uniformly heated, and not for 3D heat diffusion of the heat wave when reflecting back from the defect. The difference is even more pronounced in case of CFRPs with significantly higher in-plane thermal conductivity (along the fibres).

In this section, performance of the introduced modulated waveforms for inspection of CFRPs is evaluated based on FE simulation of the 3D heat diffusion through the laminate's thickness. Realistic conditions are considered, including the heat dissipation to the surrounding environment (radiation and convection), the non-uniform heating induced by the optical source and more importantly the measurement noise of infrared camera.

3.1 FE model of a defected CFRP and corresponding thermal phase spectrum

A 10 plies thick $[0]_{10}$ CFRP laminate as schematically shown in Figure 5(a) (equivalent to the one shown in Figure 1(a)) is modeled by Abaqus/CAE using 41,805 brick elements (DC3D20) with quadratic shape functions. The top ply is modelled by a graded mesh of two element layers (such that the thickness of the top layer is half of the bottom layer) and the lower plies are modelled with a single element layer. The graded mesh of the top ply is needed for adequate calculation of the surface temperature during fast thermal events [37] (e.g. when the heating amplitude experiences sudden changes during a modulated waveform). The assumed unidirectional lay-up (along the x-axis) is to emphasize the influence of CFRP's anisotropic thermal diffusivity. The laminate includes 6 interply defects (i.e. delaminations) defined as 5 mm wide square interfaces with nodal disbond (i.e. no thermal interaction). Temperature-dependent thermal properties are assumed for the unidirectional CFRP [35] with room temperature (25°C) diffusivity $\alpha_x = 5.39 \times 10^{-6}\,\mathrm{m^2/s}$ and $\alpha_z = \alpha_y = 6.16 \times 10^{-7}\,\mathrm{m^2/s}$ along and perpendicular to the fibers, respectively.

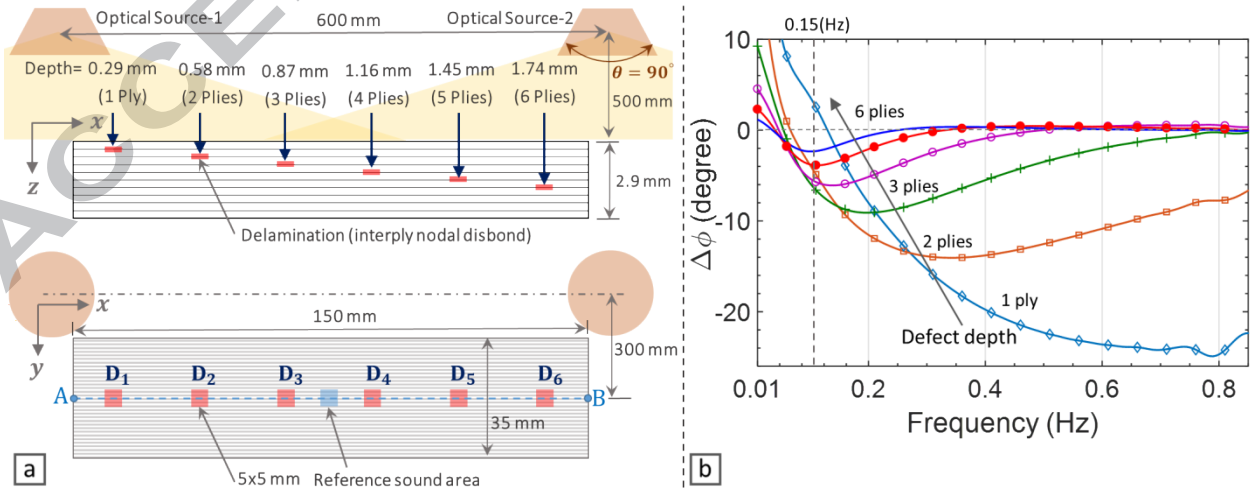

Figure 5: (a) Schematic presentation of simulated CFRP laminate $[0]_{10}$ and relative position of optical sources, and (b) corresponding spectrum of defect-induced phase contrast at inspection surface ($z = 0$)

The non-uniform heating induced by the optical source is modelled by a Gaussian distribution of the heat flux H throughout the sample's surface in xy-plane [37], as follows:

$$H(x,y) = P\left(\frac{2e}{\pi(z_0 \tan 0.5\theta)^2}\right)\exp\left(-2\frac{(x-x_0)^2+(y-y_0)^2}{(z_0 \tan 0.5\theta)^2}\right) \quad (31)$$

where P, θ and (x_0, y_0, z_0), respectively, are the heating power, the field angle and the coordinates of the optical source, and $e = 0.9$ is the assumed uniform coefficient of emissivity of the inspection surface. Equation 31 distributes 95% of the heating power over the projection field of the optical source in xy-plane (i.e. a radius $r = z_0 \tan 0.5\theta$). Two optical sources, each with heating power $P = 2$ kW and field angle $\theta = 90^{\circ}$, are assumed at a stand-off distance of 500 mm from the sample and at an offset of 300 mm from its centerline to induce an asymmetric heating pattern (see Figure 5(a)). Moreover, thermal interactions of the sample's external faces with the ambient, through radiation and convection, are taken into account. For more details concerning the FE model, the reader is referred to [37].

A minimum output solution frame rate of 25 Hz is defined for sufficient accuracy when post-processing the thermal data through matched filtering. The calculated thermal response is then degraded with Gaussian white noise with a temporal standard deviation of 20 mK equal to the noise equivalent differential temperature (NEDT) of a high-end infrared camera. Finally, the AC component of the thermal response (i.e. $\tilde{T}(t)$) required for matched filtering purpose, is calculated at each node by subtracting the corresponding DC component estimated as a polynomial interpolant. A 5 mm wide square area at the center of the sample (see Figure 5(a), bottom side) is selected and its mean value is used as a reference to determine the contrast of calculated phase and lag.

The phase spectrum of defects is calculated by FFT of the thermal response subject to an ultra-wideband sweep excitation (1-0.01 Hz, 200 s). This phase spectrum is shown in Figure 5(b) after smoothening by Savitzky–Golay filter. Comparing the two phase spectrums (see Figure 1(b) and Figure 5(b)) reveals two major differences caused by the anisotropic 3D heat diffusion. Firstly, the frequency corresponding to the maximum phase contrast significantly varies with the defect depth, particularly for shallower defects. Secondly, a positive phase contrast is evident at relatively low frequencies leading to an initial blind frequency before reaching the maximum phase contrast. In fact, the heat wave reflected from the defect (which normally contributes to a delayed peak at the surface) is dominantly dissipated through lateral heat diffusion at long cycles of relatively low frequencies.

According to the phase spectrum shown in Figure 5(b), the frequency 0.15 Hz (with poor phase contrast of deep defects in 1D thermal response) leads to a very good phase contrast over the depth range of interest. Figure 6 presents the thermograms of the top surface at two different time instances subject to harmonic excitation at this frequency, before and after adding noise.

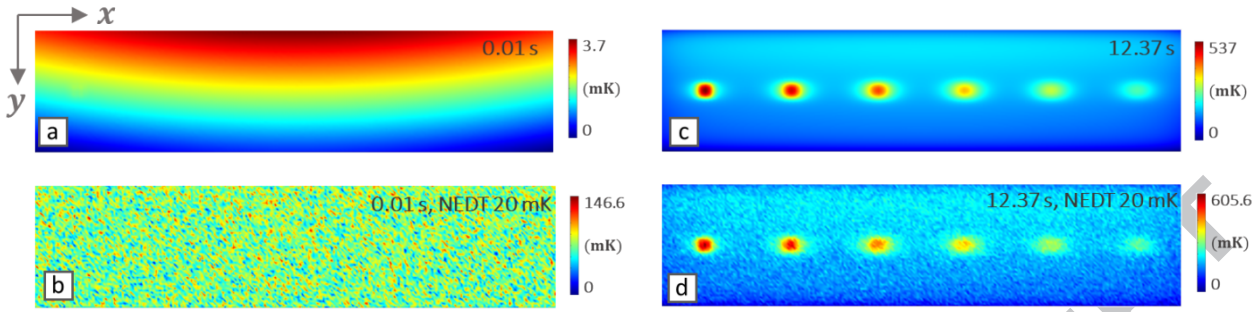

Figure 6: Thermograms obtained at different time instances (a,b) 0.01 s and (c,d) 12.37 s ; (a,c) raw thermograms, (b,d) thermograms degraded by white Gaussian noise equivalent to NEDT of 20 mK , subject to harmonic excitation 0.15 Hz (the colorbar limits indicate the absolute range of temperature gradient)

The first time instance 0.01 s (see Figure 6(a,b)) corresponds to the first iteration of the FE simulation and represents the non-uniform heating induced by the optical sources. The second time instance 12.37 s (see Figure 6(c,d)) indicates the thermal response at the presence of thermal contrast induced by all defects showing dominant lateral heat diffusion along the fibres (in x-axis). It also presents the temperature gradient of the sound area due to the non-uniform heating pattern and the lateral heat dissipation through the edges.

In the following sections, depth resolvability of the various considered modulated waveforms (Figure 2) is evaluated at multiple central frequencies. Other than the optimal excitation frequency 0.15 Hz (which is of course not known a priori in an actual infrared thermography experiment), two other central frequencies 0.4 Hz and 0.8 Hz are picked which are adjacent to the blind frequencies corresponding to the defects at 5 and 3 plies depth, respectively (see Figure 5(b)).

3.2 Depth resolvability of Barker binary coded waveform

Initially, Barker binary coded waveform (which according to the results of section 2 showed highest depth resolvability and peak-sidelobe-level) is applied and the resultant CC-phase and CC-lag are respectively shown in Figure 7(a-c) and (d-f) for the three central frequencies 0.15, 0.4 and 0.8 Hz. Each section of Figure 7 includes (i) a top subsection showing the contour map of calculated quantity (phase or lag) and (ii) a bottom subsection showing the curve corresponding to the gradient of contrast along the centerline of defects. In order to evaluate the performance of the Barker coded waveform, the phase of LT at the same central frequency is also added to the bottom side of Figure 7(a-c)). It is noteworthy that to achieve adequate time resolution in the calculation of CC-lag (only), the calculated thermal response is resampled from 25 Hz to 125 Hz (see the inset of Figure 7(a-c)), while the CC-phase is insensitive to this resampling. A Hanning window function is applied for reducing peak-sidelobe-level (function W in Equation 13) only when calculating CC-lag, as windowing proved to reduce the depth resolvability of the CC-phase.

As demonstrated by Figure 7(a,d), all defects are competently detected through both CC-phase and CC-lag at the optimal central frequency 0.15 Hz. However, LT shows a better phase contrast compared to Barker coding. The phase contrast of LT and Barker coding converge to each other at the deep defect D6 (see Figure 7(a)). Moreover, the CC-lag does not consistently reduce by the depth of the defect and shows an increasing trend between shallow defects D1 to D2 (see Figure 7(b)). This is explained by the initially positive phase contrast of D1 at 0.15 Hz as observed in Figure 5(b).

At the higher central frequency 0.4 Hz, CC-phase provides good contrast down to D5 (Figure 7(b)) while CC-lag has lower depth resolvability down to D4 (Figure 7(e)). As evidenced by the magnified presentation of data in the inset of Figure 7(b), the frequency 0.4 Hz is a bit over the blind frequency of D5 as it leads to a minor positive phase contrast of LT phase at this defect and further at D6. The Barker coded waveform results in a distinctively high phase contrast at D5, though does not improve phase contrast at D6. Likewise, the highest central frequency 0.8 Hz shows a higher depth resolvability of CC-phase down to D4 (Figure 7(c)) compared to CC-lag down to D2 (Figure 7(f)). The inset of Figure 7(c) clearly confirms that D3 which is transparent to LT phase at its blind frequency 0.8 Hz, provides a very good contrast when inspected by a Barker coded waveform at the same frequency.

Overall, Figure 7 demonstrates the robustness of CC-phase subject to a Barker coded waveform, in the detection of relatively deep defects that have poor or no phase contrast in LT (i.e. when approaching blind frequency). Moreover, it clearly shows the higher depth resolvability of the CC-phase and its lower sensitivity to the sampling frequency of thermal data, compared to CC-lag. However, it should be noted that Barker coded waveform failed to outperform LT at a frequency at which *absolute value* of phase contrast (see Figure 5(b)) is approaching its maximum (e.g. D1 at 0.8 Hz or D5 at 0.15 Hz), or when it shows an increasing trend with respect to frequency (e.g. D1 at 0.4 Hz, or D2 at 0.15 Hz). This can be explained by the relatively wideband characteristic of modulated waveforms (compared to LT) which naturally results in a shared contribution of the corresponding spectrum to the resultant CC-phase.

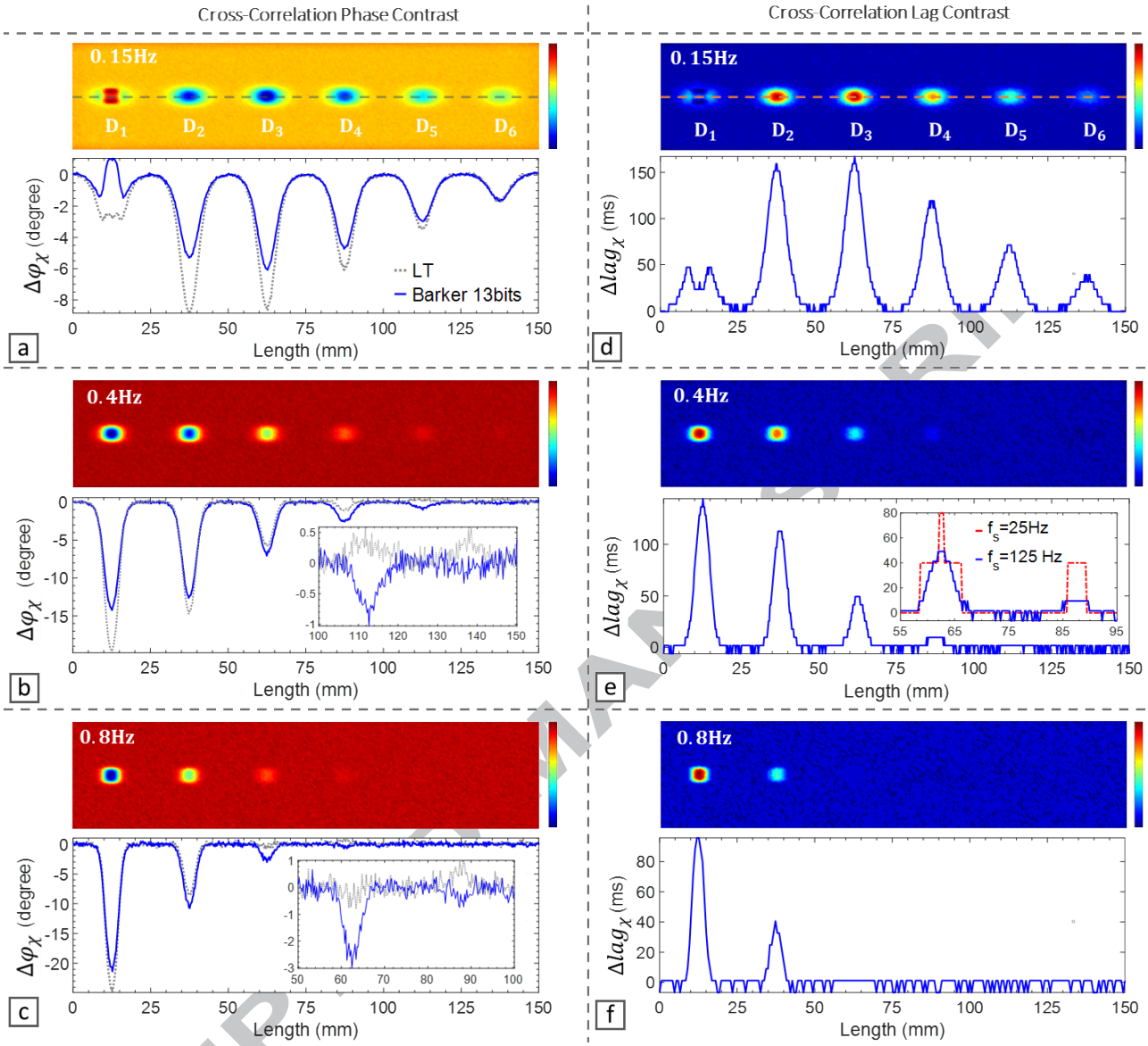

Figure 7: Calculated (a-c) CC-phase (at original 25 Hz sampling rate of FE solution) and (d-f) CC-lag (at resampled rate 125Hz) subject to a 13 bits Barker coded waveform at multiple central frequencies (a,d) 0.15 Hz, (b,e) 0.4 Hz and (c,f) 0.8 Hz ; (bottom side curves present the magnitude of contrast along the centerline of defects i.e. line AB in Figure 5(a))

Furthermore, in order to investigate the impact of DC removal procedure on the depth resolvability, thermal response to a pure AC Barker coded waveform (i.e. with zero-mean amplitude) is also calculated at 0.4 Hz. Practically, this can be done by an excitation source capable of applying the required bi-polar (heating and cooling) load. Figure 8(a) shows the good agreement of the estimated AC response (after removing a 4th order interpolant as the mean DC component) compared to the response subject to an AC excitation.

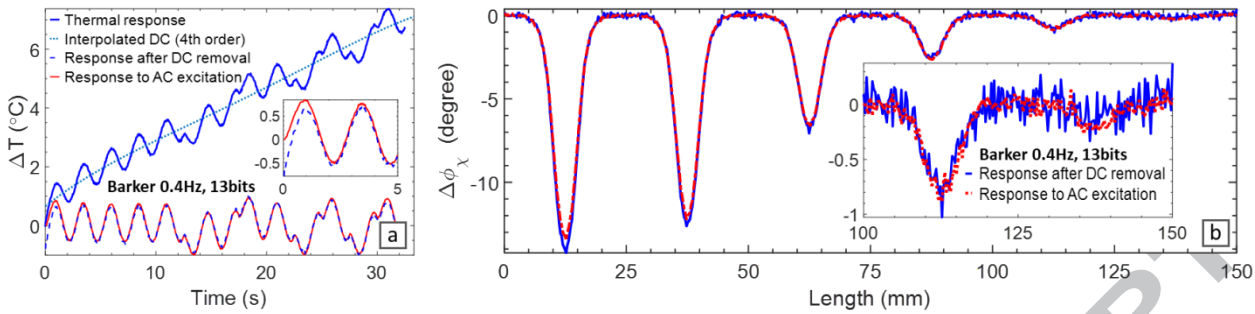

Figure 8: Estimated AC response (by interpolant DC removal) compared to accurately calculated response subject to a pure AC excitation for 13 bits Barker coded waveform; (a) thermal response and (b) corresponding CC-phase contrast along the centerline of defects (line AB in Figure 5(a))

The inset of Figure 8(a) magnifies the difference at the onset of the excitation which shows the initially negative temperature of the estimated AC response, having no physical correlation to the corresponding AC excitation in terms of amplitude (see Figure 2(b)). However, the depth resolvability of the CC-phase resultant from the estimated AC response is in good agreement with that of accurately determined AC response, as shown in Figure 8(b). The inset of Figure 8(b) shows the increased noise level originating from the DC removal process.

3.3 Depth resolvability of various modulated waveforms

In this section, depth resolvability of the modulated waveforms defined in section 2 are compared in terms of CC-phase and CC-lag. Two relatively shallow and relatively deep defects D2 and D5 are inspected at the central frequency 0.4 Hz. In fact, this frequency is in the vicinity of the frequency associated with the maximum phase contrast of D2 and close to the blind frequency of D5 (see Figure 5(b)). Likewise, defects D1 and D3 are inspected at the higher central frequency of 0.8 Hz.

Figure 9 shows the variation of corresponding CC-phase contrast along the centerline of defects (line AB in Figure 5(a)). Moreover, the resultant SNR of defects (given in the bottom right side of the curves) is calculated as:

$$\mathrm{SNR} = 20\log_{10}\frac{|\overline{\varphi}_d - \overline{\varphi}_s|}{\sigma_s} \tag{32}$$

where $\overline{\varphi}_d$, $\overline{\varphi}_s$ and σ_s are the mean value of the defected area, the mean value of the sound area and the standard deviation of the sound area, respectively. The defected area is selected as the length L_d associated with the defect induced thermal contrast (see Figure 9(d) for D5) and the sound area is an area of 10 mm wide at both sides of it.

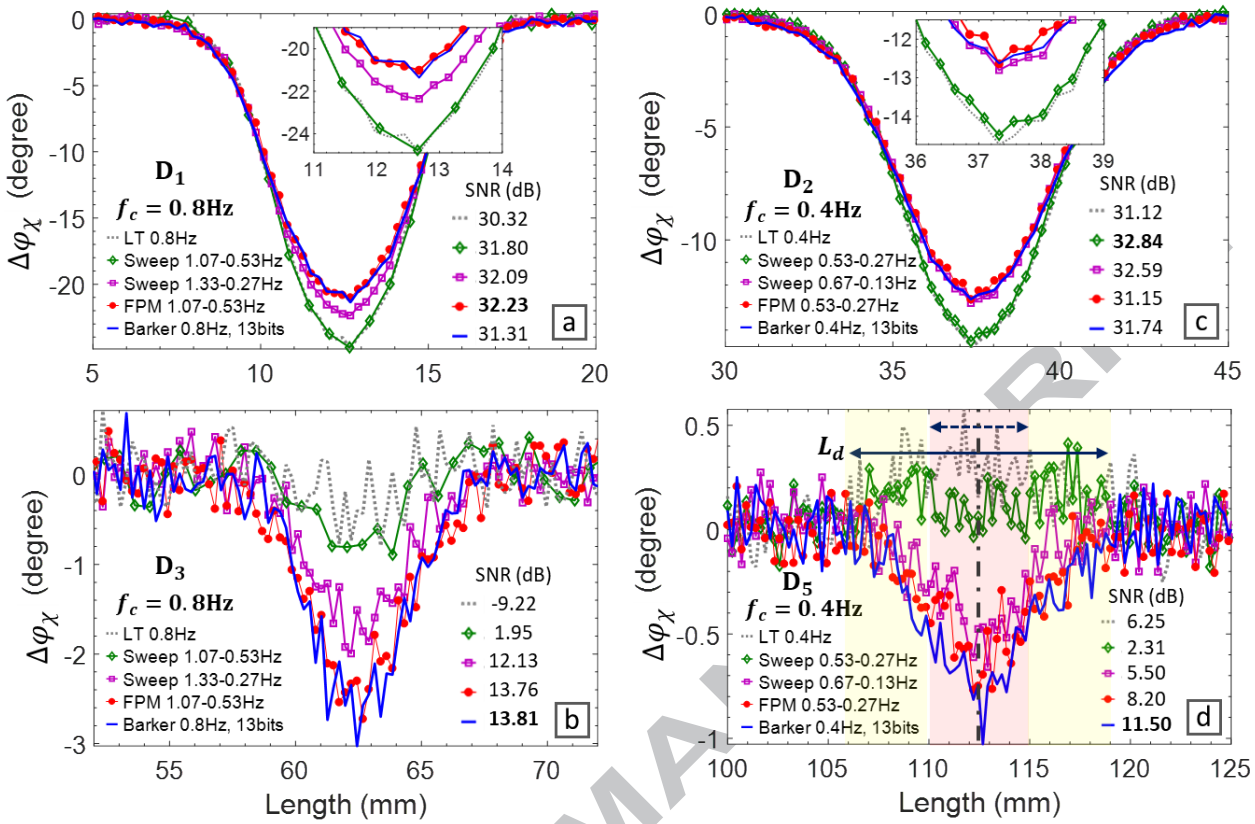

Figure 9: Gradient of CC-phase contrast at selected defects subject to different modulated waveforms along the centerline of defects (line AB in Figure 5(a)), at the central frequencies (a,b) 0.8 Hz and (c,d) 0.4 Hz

According to Figure 9 (a,c) and the phase spectrum shown in Figure 5(b), when inspecting relatively shallow defects at a central frequency in the range associated with the maximum phase contrast (i.e. D1 at 0.8 Hz, and D2 at 0.4 Hz), LT and narrowband sweep result in a larger phase contrast compared to other modulated waveforms. Nonetheless, corresponding SNRs are comparable and even slightly higher for modulated waveforms with lower contrast (i.e. FPM, wideband sweep and Barker coded) due to their lower noise level.

On the other hand, the results shown in Figure 9 (b,d) clearly confirm that when relatively deep defects are inspected at a central frequency with poor phase contrast, then modulated waveforms distinctively outperform LT (i.e. D3 at its blind frequency 0.8 Hz with no LT phase contrast, or D5 at 0.4 Hz slightly over its blind frequency with positive LT phase contrast). The performance of modulated waveforms in terms of phase contrast and SNR is correlated to their expected depth resolvability as shown in Figure 4(b). Discretely modulated waveforms (i.e. Barker coded, then FPM) have the highest depth resolvability compared to analogue frequency modulated waveforms (i.e. the wideband sweep). The narrowband sweep offers negligible improvement of SNR when inspecting at a blind frequency (see Figure 9 (b)) or even reduces the SNR compared to LT at a frequency exceeding the blind frequency (see Figure 9 (d)).

Furthermore, depth resolvability of the different modulated waveforms in terms of CC-lag is investigated. As already evidenced by Figure 7(e,f), the relatively deep defects D3 and D5 are not detectable by CC-lag at 0.8 Hz and 0.4 Hz, respectively, even after resampling the FE thermal solution from 25 Hz to 125 Hz. Hence, the two relatively shallow defects D1 and D2 are studied (Figure 10) in which slightly different CC-lag contrast is observed for the different modulated

waveforms. However, the sampling frequency of thermal data is shown to be the main limiting factor of CC-lag. The depth resolvability resolution of CC-lag (at sampling frequency125 Hz) shown in Figure 10(a,b) is clearly lower (i.e. more step-wise) than corresponding CC-phase (at sampling frequency 25 Hz) shown in Figure 9 (a,b).

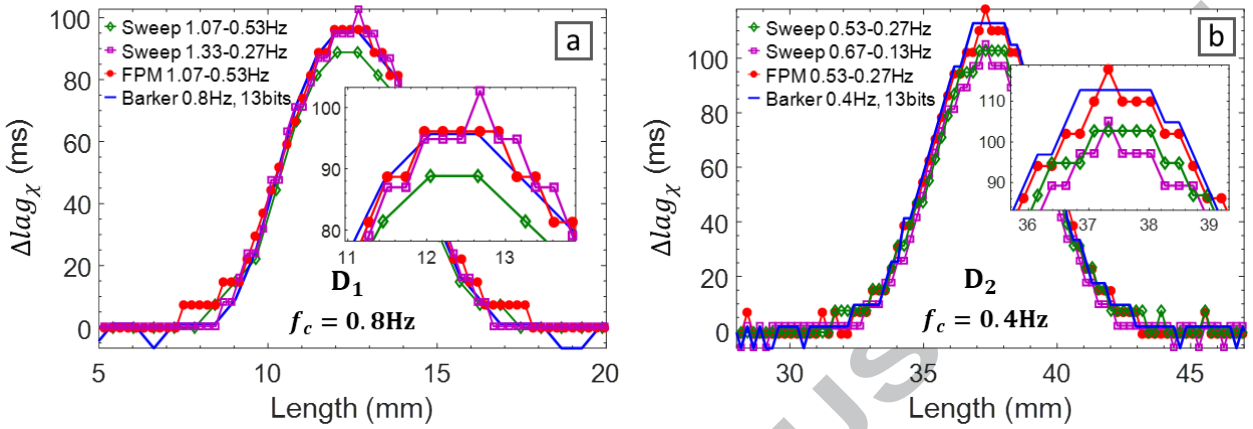

Figure 10: Gradient of CC-lag contrast subject to different modulated waveforms along the centerline of defects (line AB in Figure 5(a)); (a) D1 at central frequency 0.8 Hz and (b) D2 at central frequency 0.4 Hz; (thermal response is resampled from 25 Hz to 125 Hz for increased time resolution)

4 Conclusions

The performance of Thermal Wave Radar (TWR) in inspection of CFRPs was investigated using a simplified analytical solution to the 1D thermal problem and further by performing a 3D FE simulation with realistic boundary conditions and measurement noise. Three different waveforms with analogue frequency modulation (narrowband and wideband sweeps), discrete phase modulation (Barker coded) and a new waveform with discrete frequency-phase modulation were examined at multiple central frequencies. The latter is picked from a population of randomly generated coded waveforms based on its highest signal to noise ratio when applied to the thermal response. The emissivity-normalized quantities (i.e. lag and phase) of TWR were calculated and their depth resolvability was compared with lock-in thermography (LT).

It is shown that TWR (through modulated waveforms) generally has a higher depth resolvability compared to LT. The depth resolvability of TWR orderly increases by narrowband sweep, wideband sweep, frequency-phase modulation and ultimately by Barker binary phase coding. Increased depth resolvability of lag is evidenced by its magnified contrast throughout the depth and its widened contrast range. On the contrary, the total range of phase contrast is not increased by waveform modulation because depth resolvability of the very shallow defects is reduced by (desirably) an increased depth resolvability of deep defects. As for the frequency-phase modulated waveform, despite its comparable peak-sidelobe-level to the wideband sweep, its depth resolvability is significantly higher than the wideband sweep and in terms of phase contrast very close to the depth resolvability of the Barker coded waveform at the deepest defects

Examination of different central frequencies reveals that depth resolvability of the phase of TWR is significantly affected by the gradient of the defect-induced phase contrast in the vicinity of the chosen frequency. This obviously makes depth resolvability of the phase of TWR for certain depth range highly dependent on the total thickness of the sample (as it influences the gradient of phase contrast at the chosen frequency). If the central frequency is close to the frequency

associated with maximum phase contrast, then LT and a narrowband sweep outperform other waveforms. Otherwise, if the central frequency approaches the blind frequency of an inspection depth, then TWR outperforms LT, while narrowband sweep shows the lowest depth resolvability among the various studied waveforms.

Although analytical results show that depth resolvability of lag consistently increases by wave modulation regardless of its central frequency and the sample's thickness, its resolvability is practically limited due to the required high sampling rate. This is even worsened by the dominant lateral heat diffusion in CFRPs, which further reduces the lag contrast between the defected and sound area.

Overall, the results suggest that by selection of an arbitrary central frequency, the phase obtained from TWR technique leads to a higher probability of detection for deeper defects compared to the phase of LT at the same frequency. This gain of TWR is particularly pronounced when applying discretely modulated waveforms and when approaching the blind frequency of an inspection depth. The discrete frequency-phase modulated waveform which is introduced based on a random search, is a supreme alternative to the sweep excitation and has the potential to be further optimized for increased depth resolvability.

5 Acknowledgment

The authors acknowledge the SBO project DETECT-IV (Grant no. 160455), which fits in the SIM research program MacroModelMat (M3) coordinated by Siemens (Siemens PLM software, Belgium) and funded by SIM (Strategic Initiative Materials in Flanders) and VLAIO (Flemish government agency Flanders Innovation & Entrepreneurship). The authors also acknowledge Fonds voor Wetenschappelijk Onderzoek Vlaanderen (FWO-Vlaanderen) through grants 1148018N and 12T5418N.

References

1. Ciampa, F., P. Mahmoodi, F. Pinto, and M. Meo, *Recent advances in active infrared thermography for non-destructive testing of aerospace components.* Sensors, 2018. **18**(2): p. 609.
2. Maierhofer, C., P. Myrach, M. Reischel, H. Steinfurth, M. Röllig, and M. Kunert, *Characterizing damage in CFRP structures using flash thermography in reflection and transmission configurations.* Composites Part B: Engineering, 2014. **57**: p. 35-46.
3. Mulaveesala, R. and S. Tuli, *Theory of frequency modulated thermal wave imaging for nondestructive subsurface defect detection.* Applied Physics Letters, 2006. **89**(19): p. 191913.
4. Zhang, H., N.P. Avdelidis, A. Osman, C. Ibarra-Castanedo, S. Sfarra, H. Fernandes, T.E. Matikas, and X.P. Maldague, *Enhanced Infrared Image Processing for Impacted Carbon/Glass Fiber-Reinforced Composite Evaluation.* Sensors, 2017. **18**(1): p. 45.
5. Zhao, Y., J. Mehnen, A. Sirikham, and R. Roy, *A novel defect depth measurement method based on Nonlinear System Identification for pulsed thermographic inspection.* Mechanical Systems and Signal Processing, 2017. **85**: p. 382-395.
6. Maierhofer, C., M. Röllig, M. Gower, M. Lodeiro, G. Baker, C. Monte, A. Adibekyan, B. Gutschwager, L. Knazowicka, and A. Blahut, *Evaluation of Different Techniques of Active Thermography for Quantification of Artificial Defects in Fiber-Reinforced Composites*

Using Thermal and Phase Contrast Data Analysis. International Journal of Thermophysics, 2018. **39**(5): p. 61.

7. Marani, R., D. Palumbo, V. Renò, U. Galietti, E. Stella, and T. D'Orazio, *Modeling and classification of defects in CFRP laminates by thermal non-destructive testing.* Composites Part B: Engineering, 2018. **135**: p. 129-141.
8. Swiderski, W., *Non-destructive testing of CFRP by laser excited thermography.* Composite Structures, 2019. **209**: p. 710-714.
9. Moran, J. and N. Rajic, *Remote line scan thermography for the rapid inspection of composite impact damage.* Composite Structures, 2019. **208**: p. 442-453.
10. Müller, J.P. and R. Krankenhagen, *Optimizing thermographic testing of thick GFRP plates by assessing the real energy absorbed within the material.* Composite Structures, 2019. **215**: p. 60-68.
11. Pracht, M. and W. Swiderski, *Analysis of the possibility of non-destructive testing to detect defects in multi-layered composites reinforced fibers by optical IR thermography.* Composite Structures, 2019. **213**: p. 204-208.
12. Kuhn, E., E. Valot, and P. Herve, *A comparison between thermosonics and thermography for delamination detection in polymer matrix laminates.* Composite Structures, 2012. **94**(3): p. 1155-1164.
13. Ibarra-Castanedo, C. and X. Maldague, *Pulsed phase thermography reviewed.* Quantitative Infrared Thermography Journal, 2004. **1**(1): p. 47-70.
14. Chatterjee, K., S. Tuli, S.G. Pickering, and D.P. Almond, *A comparison of the pulsed, lock-in and frequency modulated thermography nondestructive evaluation techniques.* NDT & E International, 2011. **44**(7): p. 655-667.
15. Almond, D.P., S.L. Angioni, and S.G. Pickering, *Long pulse excitation thermographic non-destructive evaluation.* NDT & E International, 2017. **87**: p. 7-14.
16. Wang, Z., G. Tian, M. Meo, and F. Ciampa, *Image processing based quantitative damage evaluation in composites with long pulse thermography.* NDT & E International, 2018. **99**: p. 93-104.
17. Badghaish, A.A. and D.C. Fleming, *Non-destructive inspection of composites using step heating thermography.* Journal of composite materials, 2008. **42**(13): p. 1337-1357.
18. Mulaveesala, R., J.S. Vaddi, and P. Singh, *Pulse compression approach to infrared nondestructive characterization.* Review of Scientific Instruments, 2008. **79**(9): p. 094901.
19. Tabatabaei, N. and A. Mandelis, *Thermal-wave radar: A novel subsurface imaging modality with extended depth-resolution dynamic range.* Review of Scientific Instruments, 2009. **80**(3): p. 034902.
20. Tabatabaei, N., A. Mandelis, and B.T. Amaechi, *Thermophotonic radar imaging: An emissivity-normalized modality with advantages over phase lock-in thermography.* Applied Physics Letters, 2011. **98**(16): p. 163706.
21. Tabatabaei, N. and A. Mandelis, *Thermal coherence tomography using match filter binary phase coded diffusion waves.* Physical review letters, 2011. **107**(16): p. 165901.
22. Tabatabaei, N. and A. Mandelis, *Thermal coherence tomography: Depth-resolved imaging in parabolic diffusion-wave fields using the thermal-wave radar.* International Journal of Thermophysics, 2012. **33**(10-11): p. 1989-1995.
23. Kaiplavil, S. and A. Mandelis, *Truncated-correlation photothermal coherence tomography for deep subsurface analysis.* Nature Photonics, 2014. **8**(8): p. 635.
24. Tavakolian, P., K. Sivagurunathan, and A. Mandelis, *Enhanced truncated-correlation photothermal coherence tomography with application to deep subsurface defect imaging and 3-dimensional reconstructions.* Journal of Applied Physics, 2017. **122**(2): p. 023103.

25. Ghali, V., S. Panda, and R. Mulaveesala, *Barker coded thermal wave imaging for defect detection in carbon fibre-reinforced plastics.* Insight-Non-Destructive Testing and Condition Monitoring, 2011. **53**(11): p. 621-624.
26. Gong, J., J. Liu, L. Qin, and Y. Wang, *Investigation of carbon fiber reinforced polymer (CFRP) sheet with subsurface defects inspection using thermal-wave radar imaging (TWRI) based on the multi-transform technique.* NDT & E International, 2014. **62**: p. 130-136.
27. Silipigni, G., P. Burrascano, D.A. Hutchins, S. Laureti, R. Petrucci, L. Senni, L. Torre, and M. Ricci, *Optimization of the pulse-compression technique applied to the infrared thermography nondestructive evaluation.* NDT & E International, 2017. **87**: p. 100-110.
28. Shi, Q., J. Liu, Y. Wang, and W. Liu, *Study on the Detection of CFRP Material with Subsurface Defects Using Barker-Coded Thermal Wave Imaging (BC-TWI) as a Nondestructive Inspection (NDI) Tool.* International Journal of Thermophysics, 2018. **39**(8): p. 92.
29. Laureti, S., G. Silipigni, L. Senni, R. Tomasello, P. Burrascano, and M. Ricci, *Comparative study between linear and non-linear frequency-modulated pulse-compression thermography.* Applied Optics, 2018. **57**(18): p. D32-D39.
30. Arora, V. and R. Mulaveesala, *Pulse compression with Gaussian weighted chirp modulated excitation for infrared thermal wave imaging.* Progress In Electromagnetics Research, 2014. **44**: p. 133-137.
31. Burrascano, P., S. Laureti, L. Senni, and M. Ricci, *Range Sidelobes Reduction for Pulse-Compression NDT based on Reactance Transformation*, in *Circuits and Systems (ISCAS), 2018 IEEE International Symposium on*. 2018, IEEE. p. 1-5.
32. Burrascano, P., S. Laureti, and M. Ricci, *The Reactance Transformation for Near Sidelobes Reduction: A Comparison of Windowing Techniques*, in *2018 15th International Conference on Synthesis, Modeling, Analysis and Simulation Methods and Applications to Circuit Design (SMACD)*. 2018, IEEE. p. 37-40.
33. Nathanson, F.E., J.P. Reilly, and M.N. Cohen, *Radar design principles-Signal processing and the Environment.* NASA STI/Recon Technical Report A, 1991. **91**.
34. Mahafza, B.R., *Radar Systems Analysis and Design Using MATLAB Third Edition*. 2016: Chapman and Hall/CRC.
35. Joven, R., R. Das, A. Ahmed, P. Roozbehjavan, and B. Minaie, *Thermal properties of carbon fiber-epoxy composites with different fabric weaves.* SAMPE, Charleston, SC, 2012.
36. Nash, G., *Preliminary report on pulse compression waveforms and their application to waveform agility*. 2004, Defence Science and Technology Organisaion Salisbury (AUSTRALIA) Systems Sciences Laboratory.
37. Hedayatrasa, S., J. Segers, C. Tellez, J. Andres, W. Van Paepegem, and M. Kersemans, *On Efficient FE Simulation of Pulse Infrared Thermography for Inspection of CFRPs*, in *14th Quantitative InfraRed Thermography Conference*. 2018.